

FPGA implementation of 500-MHz high-count-rate high-time-resolution real-time digital neutron–gamma discrimination for fast liquid detectors*

Hui-Yin Shen,¹ Jing-Long Zhang,^{1,†} Jie Zhang,² and Jian-Hang Zhou¹

¹*College of Nuclear Technology and Automation Engineering,
Chengdu University of Technology, Chengdu 610059, China*

²*Southwestern Institute of Physics, P.O. Box 432, Chengdu 610041, China*

Fast neutron flux measurements with high count rates and high time resolution have important applications in equipment such as tokamaks. In this study, real-time neutron and gamma discrimination was implemented on a self-developed 500-Mcps, 12-bit digitizer, and the neutron and gamma spectra were calculated directly on an FPGA. A fast neutron flux measurement system with BC-501A and EJ-309 liquid scintillator detectors was developed and a fast neutron measurement experiment was successfully performed on the HL-2M tokamak at the Southwestern Institute of Physics, China. The experimental results demonstrated that the system obtained the neutron and gamma spectra with a time accuracy of 1 ms. At count rates of up to 1 Mcps, the figure of merit was greater than 1.05 for energies between 50 keV and 2.8 MeV.

Keywords: Neutron–gamma discrimination; Liquid scintillation detector; Real-time spectrum analyzer

1. INTRODUCTION

Fast neutron flux measurements have important applications in various fields, including neutron monitoring [1], fusion research [2], homeland defense, and nuclear security [3]. Neutron sources are always accompanied by de-excitation gamma rays, which are difficult to discriminate from neutrons [4]. Therefore, detectors and readout electronics with neutron–gamma discrimination capabilities are required.

An organic liquid scintillator is a luminous substance, such as biphenyl, dissolved in toluene, xylene, or other configured liquid solvents [5]. It is suitable for neutron detection because it provides high detection efficiencies, and the short time constant (typically a few ns) of its rapid scintillation provides satisfactory time resolution [6]. Compared with the methods of neutron moderation represented by BF₃ proportional counters [7] and the ²³⁵U fission chamber [8], these crystals are effective for neutrons and γ -rays. Appropriate algorithms and well-matched electronics are necessary for final neutron measurements. Because fast neutron detectors such as BC-501A [9] and EJ-309 [10] are used, the output signal pulse is generally narrow, and the rise time of these detectors is $t_r \leq 20$ ns. Therefore, the readout electronics require a high sampling rate and acquisition accuracy to achieve a satisfactory discrimination effect.

The classical methods developed for discriminating waveform characteristics include the distance, area, and angle gradient methods. Compared with these methods, charge comparison (a type of area method) is more robust to the sampling rate and sampling accuracy. Its greater robustness, simple calculations, and satisfactory figure of merit (FOM) make it particularly suitable for real-time computing [11].

Using pulse-shape discrimination (PSD) methods, previous studies have focused on offline analysis. Thus, signals were

first acquired with an electronic device, and subsequently, MATLAB (or Python) algorithms were written for offline analysis [12, 13]. In certain high-radiation fields, the total data rate can be extremely high. Such data is difficult to store and process offline, and its massive size affects the efficiency of the analysis [14], thereby limiting its contribution to the subsequent study of neutron discrimination. Currently, FPGA online algorithms have been implemented by Le Cai et al. [15], Ye et al. [16], and Liu [17]. At high sampling rates, the DRS4 fails to achieve continuous sampling of the signal; thus, the count rate fails to reach a high level. The online algorithms of Ye and Liu are not equipped with liquid scintillator detectors; thus, their application in high-count-rate radiation fields has not been reported. Fernandez et al. developed FPGA firmware and software for the ITER neutron camera, where high sampling rates and high-precision electronics allow online neutron gamma discrimination (neutron gamma source generated by CAEN emulator). However, practical applications on ITER have not been reported [19, 20]. The APV8102 system of TechnoAP, with 1 GHz 14 bit ADC and FPGA was experimented on LHD; however, the neutron gamma discrimination of this system was significantly worse at count rates above 100 kcps. Further, its temporal resolution was not sufficiently high [21]. The application of a high-count-rate neutron flux measurement system to tokamaks aids our understanding of the physics of energetic ions in fusion plasmas [22].

However, because pipelined discrimination is difficult to implement in an FPGA under these conditions, few reports and technical details on real-time FPGA discrimination algorithms at high sampling and counting rates are available.

In this study, a high-count-rate (> 1 Mcps) and high-time-resolution (1 ms) real-time digital neutron–gamma discriminator was developed. To meet data processing requirements at high count rates, the readout electronics output data in list mode and directly sent spectrum statistics to the computer at regular intervals.

This paper describes the architecture of the FPGA firmware, including the pileup rejection, baseline calculation, peak detection, integration unit, PSD calculation, and pulse

* Supported by the National Magnetic Confinement Fusion Program of China (No. 2019YFE03020002) and the National Natural Science Foundation of China (No. 12205085 and 12125502)

† Corresponding author, zhangjinglong17@cdut.edu.cn

height analyzer (PHA). Next, the related experiments and results are presented. The results obtained during the plasma discharge process, which can be used as a reference for the discrimination effect at high count rates, are also provided.

2. METHODOLOGY

The digital neutron–gamma discrimination system (NGDS) is applicable to strong radiation fields containing n/γ signals and can be implemented with real-time n/γ signal discrimination at a high count rate and time resolution. When a series of measurement parameters is assigned, the NGDS calculates the PSD value of the measured signal, performs real-time neutron and gamma amplitude spectrum statistics, and uploads the relevant data to the computer software to achieve n/γ discrimination. The NGDS can be adjusted to other liquid scintillator detectors by modifying a series of measurement parameters.

2.1. Hardware description

The hardware of the NGDS comprised three parts: a liquid scintillator detector, programmable digitizer, and computer. The liquid scintillator detector (such as EJ-309 and BC-501A, which have proven to be capable of PSD) served as a neutron detector. The digitizer provided the detector with a high negative voltage, facilitating signal acquisition under appropriate conditions. Real-time digital neutron–gamma discrimination firmware was implemented on the FPGA. The processed data were uploaded to the computer via ethernet based on the TCP protocol. Finally, the neutron–gamma discrimination results were stored and displayed via an online measurement software [see Fig. 1(a)].

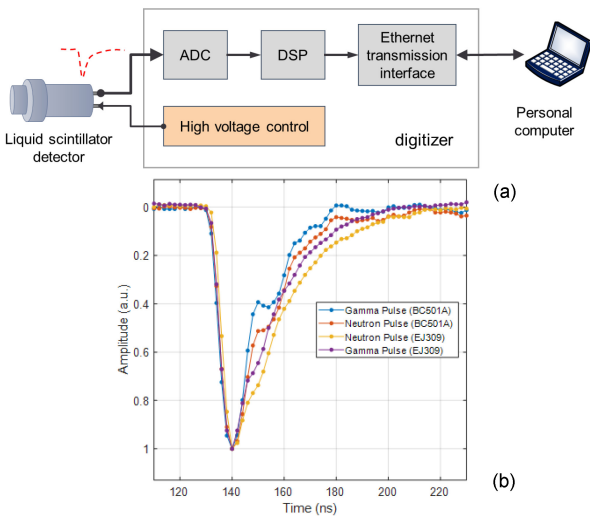


Fig. 1: (a) Block diagram of the digital NGDS. (b) Typical waveforms of the detectors BC-501A and EJ-309.

The port on the detector output directly to the digitizer without amplification. A high-speed 500-Msps, 12-bit analog-to-digital converter (ADC) was used in the NGDS for digitization. The FPGA adopted in this study was A SPARTAN-6 Xilinx; its main features are listed in Table 1.

TABLE 1: Key Parameters of the programmable digitizers.

Type	Value
Sampling rate	500 Msps
Analog-to-digital range	12 bits
Number of channels	1
Noise	<500 μ V RMS
High-voltage supply	0 to –2000 V
Input dynamic range	600 mV
Interface	Gigabit Ethernet
Transmission speed	100 Mbps

The experiment was performed using the neutron–gamma source Am-Be241 (located at Chengdu University of Technology) and the HL-2M tokamak. Typical waveforms for BC-501A and EJ-309 are shown in Fig. 1(b).

2.2. Architecture of the FPGA firmware

The FPGA in our digitizer performed real-time pulse processing, which primarily involved: (1) increasing the signal-to-noise ratio (SNR), (2) pulse triggering with a specified voltage threshold, (3) pile-up rejection, (4) acquiring the baseline value of a pulse within a specified duration, (5) acquiring the peak value of a pulse within a specified length, (6) integral calculation for a specific length, (7) PSD calculation and analysis, and (8) neutron / gamma (n/γ) pulse height analysis with a specified channel number. The firmware can be adapted to various detectors, and different software packages can be designed to meet practical requirements.

The FPGA architecture is shown in Fig. 2. The DNGS functioned in the list and spectrum modes, which processed data differently and corresponded to pulse information calculation and data analysis, respectively. Meanwhile, the waveform acquisition firmware inside the FPGA acquired the original waveform for offline analysis independent of the two measurement modes. The triggering and sampling options were controlled to collect the original pulse signal, which was necessary for analyzing the signal features. The data generated by these three modes were independently packaged and sent to the computer for different functions.

When the clock frequency for signal processing was 500 MHz, satisfying the timing requirements of the FPGA in signal pipelining was difficult. Therefore, this study used a serial-to-parallel conversion pipeline to convert a 500-MHz, 12-bit data volume into four parallel 125-MHz, 12-bit data processes. Four-channel parallel processing was a reasonable choice.

The main digital signal processing was performed in the list mode, and the essential parameters for n/γ discrimination were calculated. The signal from one of the channels was calculated as a trigger that determined the starting point of the

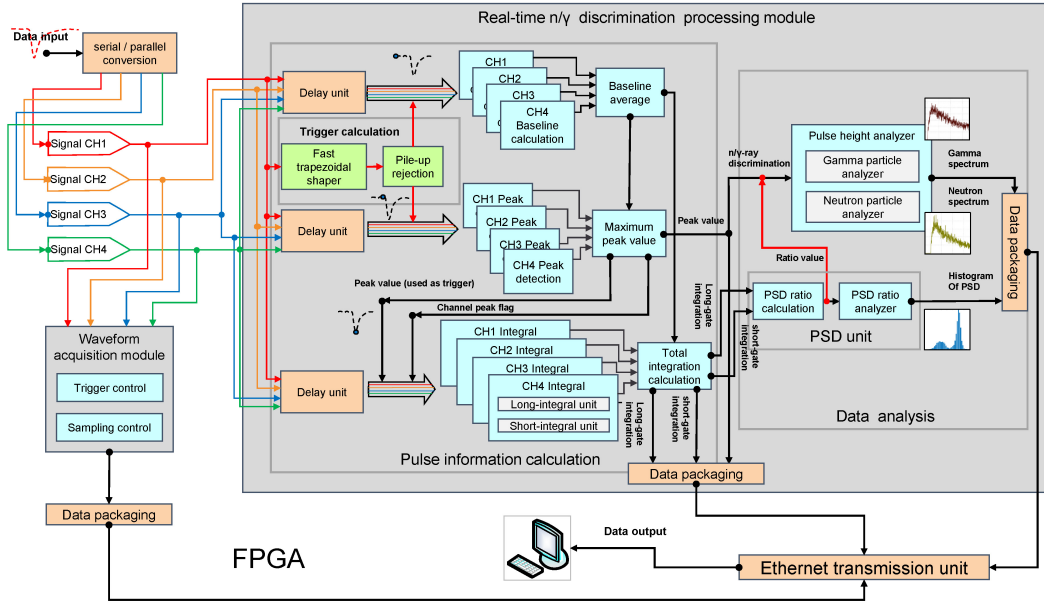


Fig. 2: Block diagram of the FPGA architecture.

baseline calculation and peak detection. After the peak and baseline values were obtained, the peak was used as the trigger signal for integration. Each channel simultaneously performed real-time pulse processing, including baseline, peak, and integral calculations, and the final result was obtained after synthesis. The baseline calculation increased the SNR. After the PSD ratios were determined by the computer, the information was displayed using the software. Simultaneously, these parameters were statistically analyzed directly on the FPGA (performing the data analysis) and finally, the discriminated n - γ spectrum was obtained.

Thus, the timing requirements of the FPGA were also satisfied while implementing the 500-Msps sampling rate and utilizing the ADC performance.

2.3. Fast-trapezoidal shaper and pile-up rejection

The fast-trapezoidal shaper is a universal and flexible digital shaper that handles the tradeoff between the minimization of resolution and maximization of throughput by providing adjustable parameters for the peaking time and flat-top duration [23].

The fast-trapezoidal shaper module contains delay and subtraction units. The input signal was first divided into two branches (assigned different delays) and subtracted to form a shaped signal that was positive and then negative. The trigger signal was generated when the input signal exceeded the preset threshold [24].

At high count rates, the pulse pile-up effect became significant, influencing the pulse amplitude and reducing the resolution of the energy spectrum [25]. A pulse was generated by the trigger signal. If the width between the previous and the next pulse was less than a predefined value, the current pulse

was considered a pile-up pulse to be rejected; otherwise, it was considered an acceptance pulse.

2.4. Baseline calculation and peak detection

Baseline calculations and peak detection were triggered by a pulse flag generated by a fast trapezoidal shaper.

Before the arrival of the leading edge, the average of the signal was obtained and used as the baseline value for the pulse signal. In the peak detection module, the peak detection length was controlled by a command to accommodate different detectors. The module output the minimum (peak) signal when the predetermined upper limit of the peak detection length was reached.

2.5. Integration and PSD calculation

The charge comparison method (CCM) is an effective PSD method for performing n - γ discrimination [26, 27].

In an environment comprising mixed neutron and gamma-ray pulses, the neutrons and gamma rays produce different secondary charged particles in liquid scintillator detectors. In scintillators, the components of light pulses excited by charged particles possess different decay times. Furthermore, these particles produce different waveforms of the output light pulse, especially with regard to the intensity of the tail component, which allow their identification. Neutrons have a higher slow-tail component than gamma-rays [16, 28].

The CCM can be implemented on an FPGA through a simple integration operation, which typically involves comparing the charge integration of a current pulse over two different

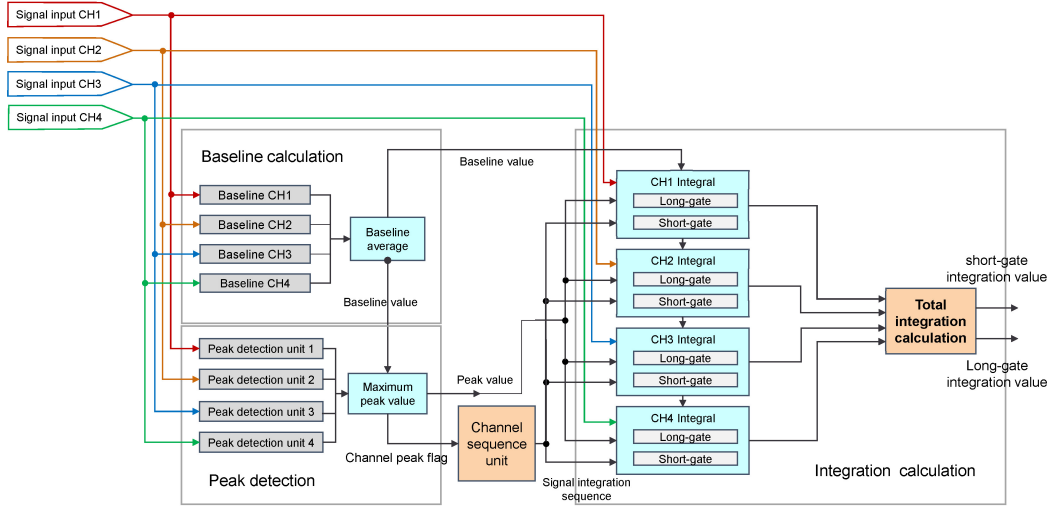


Fig. 3: Block diagram for four-channel parallel-processing.

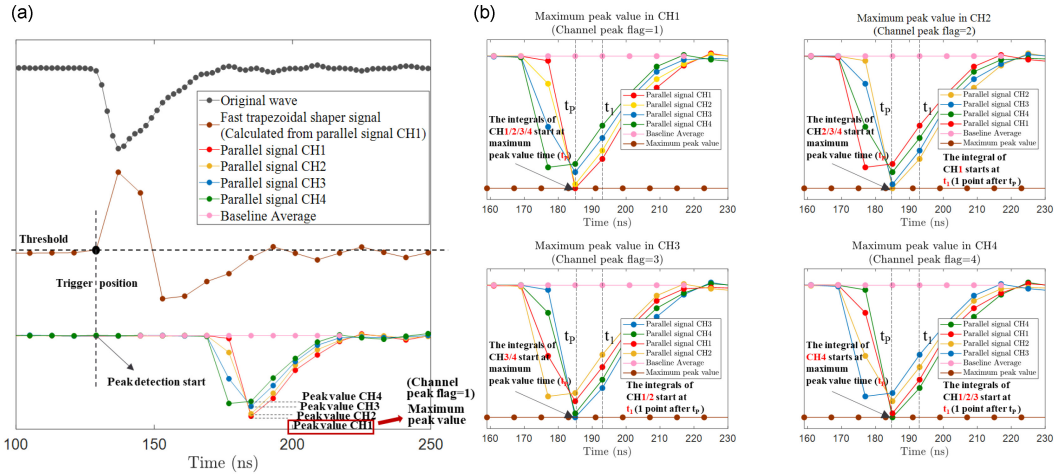


Fig. 4: (a) Four-channel parallel processing in trigger calculation and peak detection, showing the original waveform and parallel signals with points marked every 2 ns (500 Mps) and every 8 ns (125 Mps), respectively. (b) Four-channel parallel processing in integration, with the starting positions of the four channels (CH1-4) for integration in four situations (channel peak flags from 1 to 4).

time intervals. For practical calculations, the PSD is defined as the ratio of the short integral to the long integral at the trailing edge of the current pulse. The integration was divided into long-gate (I_S) and short-gate (I_L) integrations, depending on the integration length.

Integration was performed after peak detection. I_S begins at the peak point of the pulse (T_P) and extends to a position before the end of the trailing edge. I_L starts at the same position as I_S and possesses a greater integration width. The longer decay time of neutron pulses facilitates discrimination between neutrons and gamma rays. These two integral regions can be easily implemented and adjusted by sending commands to the FPGA.

The integral operation is followed by the PSD ratio calculation. The PSD ratio is defined as follows:

$$PSD = \frac{I_S}{I_L}. \quad (1)$$

The PSD ratio calculation unit was implemented using an eight-bit divider that calculated the ratio of I_S to I_L for each channel in real time. Finally, PSD results were transferred to the PC via a gigabit ethernet link. A common FOM method was used to evaluate the n/γ -ray discrimination effectiveness [29–31]. The FOM is defined as:

$$FOM = \frac{\Delta X}{\delta_{\gamma} + \delta_{n}}, \quad (2)$$

where ΔX is the distance between the neutron and gamma ray peaks, while δ_{gamma} and δ_{neutron} represent the full width at half maximum (FWHM) of each corresponding peak. To calculate the FOM values for the analysis, the PSD values of n/γ were fitted with two Gaussian distributions[15].

The selection of I_S and I_L widths significantly affected the FOM. As shown in Eq. 1, if I_S width is too small at a constant I_L width, the deviation in the PSD value obtained is larger (greater impact of the noise received); furthermore, a significantly long region along the trailing edge will not be utilized. In contrast, if the I_S width is set too large (close to the I_L width), the final FOM value will be smaller (loss of neutron–gamma differences), yielding PSD values close to one. An excessive I_L width inevitably causes noise near the baseline, which results in larger PSD value deviations and increases the calculation workload and computation time. This adversely affects pulse discrimination calculations at high count rates. A small I_L width (close to the I_S width) results in poor FOM values.

2.6. Spectrum analyzer

The PSD unit and PHA are important components of data analysis. The PSD values were stored by the ratio analyzer module as a histogram with 256 channels, whereas a pulse height histogram (1–1024 channels for gamma rays and 1025–2048 channels for neutrons) was stored by the PHA. The PSD ratio was calculated using the divider and fed into the two PHAs for discrimination. In this process, each pulse signal classified by the PSD value was completed once by the digitizers, and the computer interface displayed the data from the PHA and PSD analyses. The size of the data and transfer rate depended on the upload interval, which maximized the speed of the FPGA chips and implemented high count-rate measurements while reducing the dependence on network speed.

2.7. Four-channel parallel processing

To meet the timing requirements of the FPGA under the conditions of signal pipelining, four 125-MHz parallel pipeline processes were used with 12-bit data. Four-channel parallel processing was performed for baseline calculation, peak detection, and integral calculation, as shown in Fig. 3. After the baseline values were calculated separately for each of the four groups in the baseline calculation module, the average value was again calculated in the baseline average unit. The result was used as the baseline value.

The signal of one channel (e.g., CH1) was calculated using the fast-trapezoidal shaper module to generate a trigger signal using over-threshold triggering. Within the peak detection module, each unit obtained the peak value of each pulse and the four peaks were compared in the maximum peak value unit to determine the peak value. Simultaneously, the output channel peak flag was used to determine the channel to which

the maximum peak belonged, because of its importance for the subsequent parallel integration [see Fig. 4(a)].

After the baseline was subtracted, the maximum peak was used as the trigger signal for integration. The channel sequence unit controlled the order of integration between the four signals according to the value of the channel peak flag (from 1 to 4). Thus, the channel where the maximum peak is located is integrated first, as shown in Fig. 4(b).

In the integral calculation unit, the results of the four-channel integration were added to output the total short- and long-gate integration values.

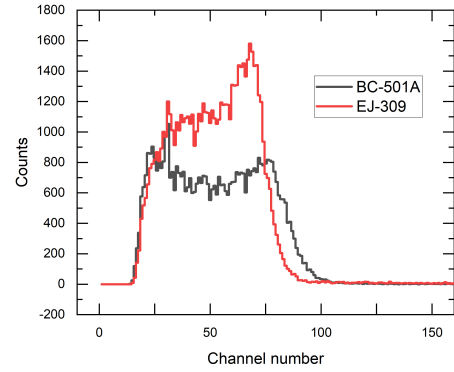


Fig. 5: Gamma energy spectrum of Cs-137 obtained using BC-501A and EJ-309.

2.8. Data transfer

Because the list mode was trigger-based, the amount of data and the transmission rate depended on the count rate of the source. In this process, more detailed particle information might be obtained; however, this was limited by the data transfer rate from the FPGA. This method relies on the network speed, which is unsuitable for measurements at high count rates (usually above 1 Mcps). The data transfer speed in the list mode was influenced by the count rate. One package (with a size of 27 bytes) corresponded to the calculated data of one particle containing the arrival time of the pulse, integration value, count value, and amplitude information. When the count rate was 1 Mcps, the transfer rate was approximately 210 Mbps, which created high demands on the ethernet hardware. High count rates also required the storage of more data.

In the spectrum mode, all particles were continuously counted over a period of time, and the results were displayed. The size of the two packets was 6962 bytes, and the analysis results were uploaded at equal intervals until the end of the measurement. The measurement software facilitated the viewing of the analytical processes using the time-trace function. The upload time was set from 1 to 100 ms to satisfy the different time precisions. Ethernet hardware with different parameters were selected according to actual application requirements. The transmission rates were approximately 53

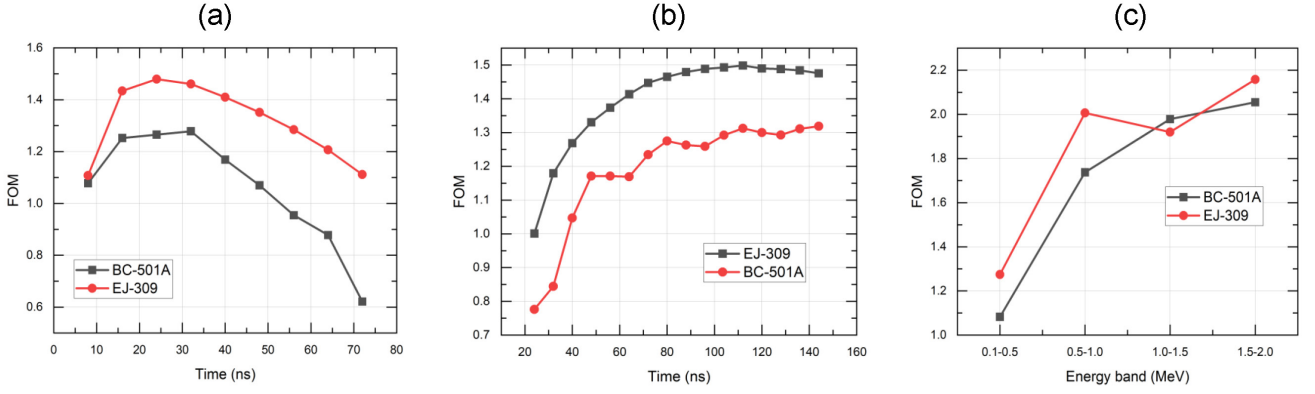


Fig. 6: Effects of (a) short-gate integral length and (b) long-gate integral length. (c) FOM measured at different energy bands.

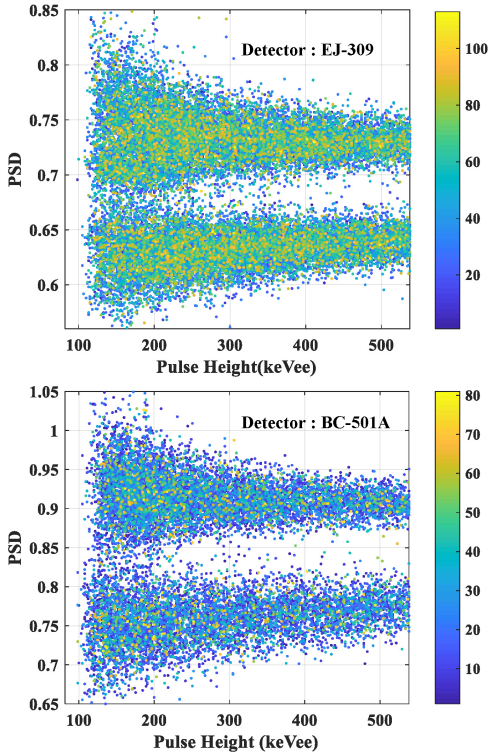


Fig. 7: Scatter plots of the PSD and pulse height with a 100-keV_{ee} threshold.

Mbps and 0.53 Mbps at high (1 ms) and low (100 ms) time precision, respectively. This resolves the limitation of network speed for high-count-rate analysis.

3. EXPERIMENTS USING AN AM-BE SOURCE

3.1. Energy calibration

A Cs-137 gamma source was used to calibrate the detector energy and perform neutron gamma discrimination at the determined energy threshold. Calibration was performed by plotting the energy spectrum of Cs-137. The response of liquid scintillator detectors to gamma rays primarily refers to energy deposition during Compton scattering. The results of the calibration, that is, the distribution of 50,456 pulse heights with the channel position for BC-501A and 67,043 for EJ-309, are shown in Fig. 5.

The Compton edge energy of Cs-137 gamma rays is 477 keV. The channel position at 75% of the Compton-edge maximum was used to calculate the calibration line[32, 33]. Thus, a correspondence was observed between the channel number and energy.

3.2. Parameter optimization

In practical applications, the different response signal characteristics of different types of scintillator detectors, necessitates the selection of the optimal parameters through a series of comparative experiments. The long- and short-gate integration lengths affect the final PSD ratios and directly determine the discrimination under the same measurement threshold. To explore the effect of different long-gate (short-gate) integration lengths on the discrimination effect and determine the optimal discrimination parameters of the detector, we used the waveform acquisition module inside the FPGA to acquire a large number of pulse signals (105,000 for BC-501A and 84,595 for EJ-309) for offline analysis in MATLAB.

Based on the typical results of previous experiments, various short-gate integration times were set with an equivalent electron energy of 300 keV_{ee} and a long gate integration time of 96 ns. As shown in Fig. 6(a), the FOM trends of the two detectors remain the same as the short-gate integration time

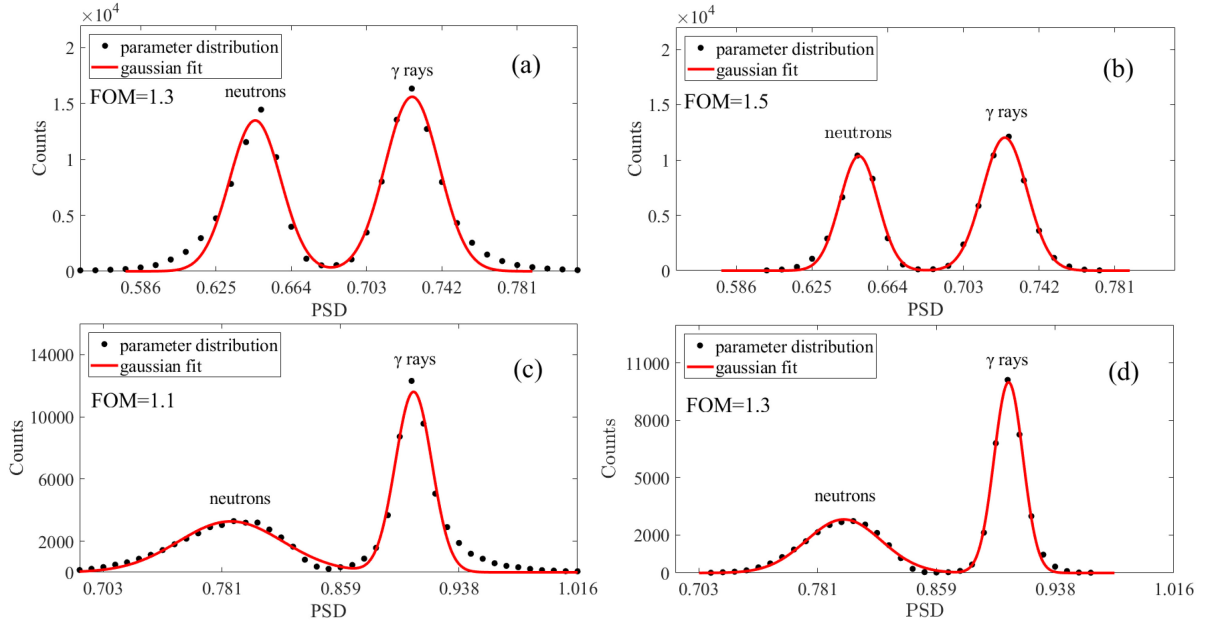


Fig. 8: PSD distributions with thresholds of (a) 100 keV_{ee} and (b) 300 keV_{ee} using EJ-309. PSD distributions with thresholds of (c) 100 keV_{ee} and (d) 300 keV_{ee} using BC-501A.

increases. The maximum FOM values are obtained at 24 ns and 32 ns for EJ-309 and BC-501A, respectively. This is not significantly different from the FOM value at 24 ns; therefore, 24 ns can be set as a suitable short-gate integration length. Fig. 6(b) shows that with a short gate integration time of 24 ns, the FOM values of the two detectors increase with the long gate integration time. The growth of the values on the two lines gradually flattens, and excessively long integration times increase the FPGA computation time, which hinders digital signal processing at high count rates. Therefore, the integration time of 96 ns was selected as the optimal value.

Through offline analysis of the waveform data, our experiments showed that 24 ns was a typical interval for a short-gate integral using these two detectors. Meanwhile, 96 ns was a typical interval for a long-gate integral that approximately covers the tail area of a pulse.

The measured FOM for the different detectors in the different energy bands are shown in Fig. 6(c). The FOM improves with increasing pulse height, resulting in a higher SNR.

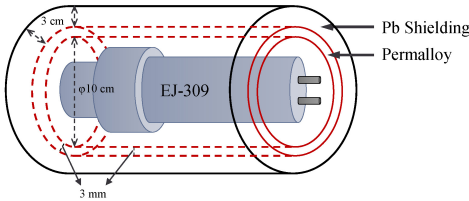


Fig. 9: Additionally shielded EJ-309.

3.3. Results for real-time pulse shape discrimination

The real-time PSD results were calculated after selecting the optimized PSD parameters. Fig. 7 illustrates the discrimination effects of the data collected in the list mode. We measured 56,031 and 34,781 pulses using the detectors EJ-309 and BC-501A, respectively, at an energy threshold of 100 keV_{ee}.

The distinction between neutrons and gamma-rays becomes evident as the energy threshold increased, as shown in Fig. 8. The PSD has a double Gaussian distribution, where the data on the left side represent the neutron pulse and its corresponding Gaussian peak, while the data on the right side represent the gamma rays. The FOM indicates the quality of particle discrimination. As the FOM increased, the fitting of the double-Gaussian distribution improved. For the detector EJ-309, the FOM values were 1.3 and 1.5 for thresholds of 100-keV_{ee} and 300-keV_{ee}, respectively. Likewise, the FOM values for BC-501A were 1.1 and 1.3 for 100-keV_{ee} and 300-keV_{ee}, respectively. These values are poorer than those of EJ-309. When the upload interval, measurement time, threshold, and other parameters were set, the real-time software simultaneously displayed the PSD curve, energy spectrum, and current count rate of the two detectors.

4. EXPERIMENTS ON THE HL-2M TOKAMAK

Two NGDS devices were developed for the experimental hall of the HL-2M tokamak at the Southwestern Institute of Physics (SWIP): one with a BC-501A detector, and the other

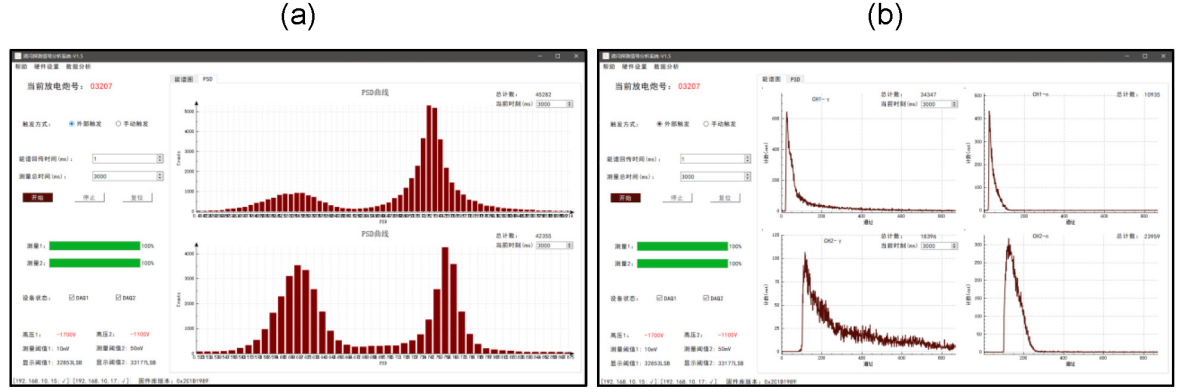


Fig. 10: Real-time measurement software interface. (a) PSD curves of BC-501A (CH1) and EJ-309 (CH2). (b) n/γ spectra of BC-501A (CH1) and EJ-309 (CH2).

with an EJ-309 detector.

Soft iron with a thickness of 20 mm and a permalloy of 5 mm were used in BC-501A for PMT magnetic shielding[34], and EJ-309 was additionally gamma-shielded and magnetically shielded. (see Fig. 9).

4.1. Software real-time discrimination display

The results obtained by both detectors were simultaneously recorded using the neutron–gamma discrimination software. Parameters such as the threshold, integration length, and measurement time were set. The software directly displayed the PSD statistical curves of the two NGDS. When the discrimination parameters of the neutrons and gamma-rays were set, their respective energy spectra were obtained at the end of the measurement (see Fig. 10). Simultaneously, a data traceback viewing function was designed in the software to review the energy spectrum information and PSD curve statistics at any moment (with a minimum time precision of 1 ms).

4.2. Performance of the NGDS

4.2.1. Waveform acquisition

The characteristics of liquid scintillation detectors must first be evaluated by acquiring and analyzing their waveforms. As shown in Fig. 11, the NGDS operates in waveform acquisition mode during plasma discharge. During the measurement within 1 μ s, the piled-up pulses were well suppressed owing to the strong shielding conditions even at high count rates, indicating that the detectors were performing in a sufficiently high and dynamic voltage range. Simultaneously, the existence of a pile-up pulse indicates the necessity of a signal processing method at high count rates.

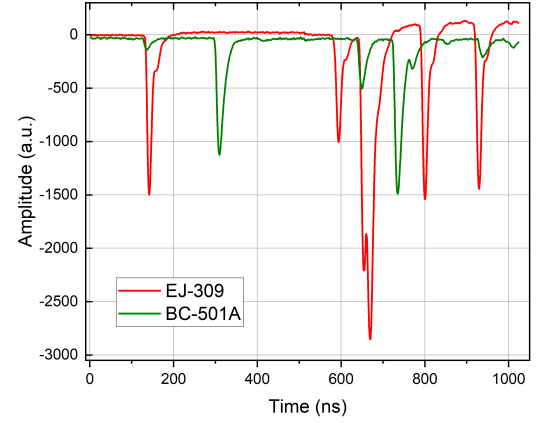


Fig. 11: Recorded waveform over a 1- μ s duration from discharge #03207

4.2.2. Neutron time traces of different neutron detection systems

For comparison with the NGDS, an HTRN_S system (including a ZnS detector), ^{235}U fission chamber (FC), and ^3He counter were placed next to the tokamak. HTRN_S system, ^3He counter, and ^{235}U fission chamber were developed for neutron yield measurements [18]. A series of measurements was obtained from different discharge numbers. Fig. 12(a) presents the time traces of the neutron count rates (corresponding to two different discharge numbers) with a temporal resolution of 1 ms. Overall, during plasma discharge, FC had the largest neutron count rate, which was approximately 2-4 times that of BC-501A during the same period. EJ-309 and HTRN_S were comparable, whereas those of BC-501A and ^3He were lower. The neutron detection efficiency of EJ-309 was approximately twice that of BC-501A during the same period; furthermore, it had a better neutron detection

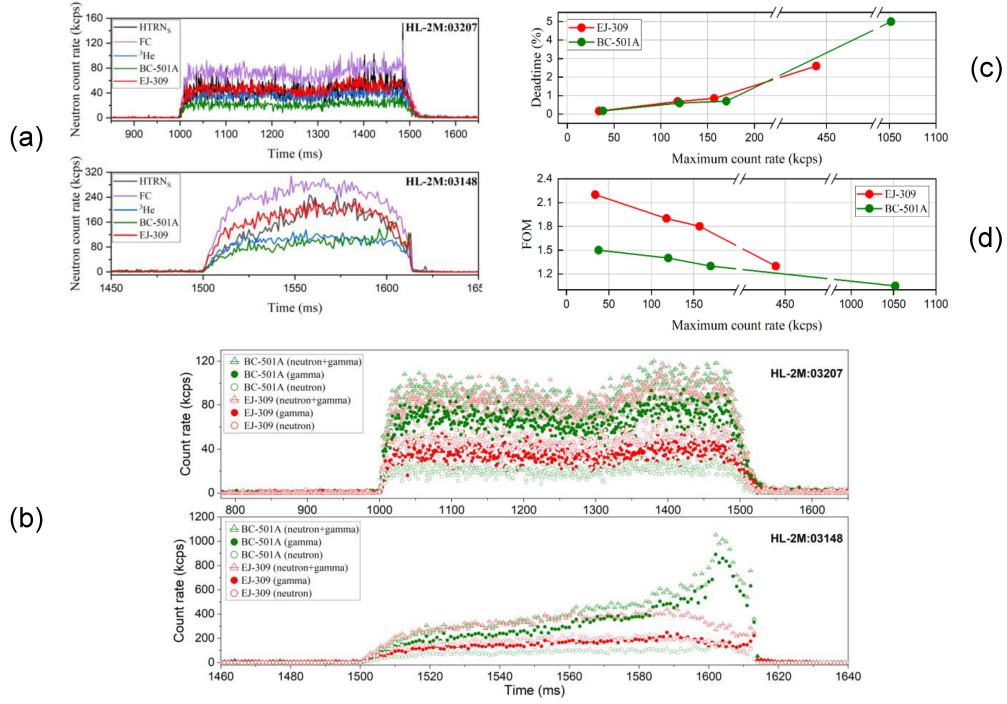


Fig. 12: (a) Time traces of the neutron count rates from discharges #03207 and #03148. (b) Time traces of the neutron and gamma count rates from discharges #03207 and #03148. (c) Dead time and (d) FOM with different maximum count rates using EJ-309 and BC-501A.

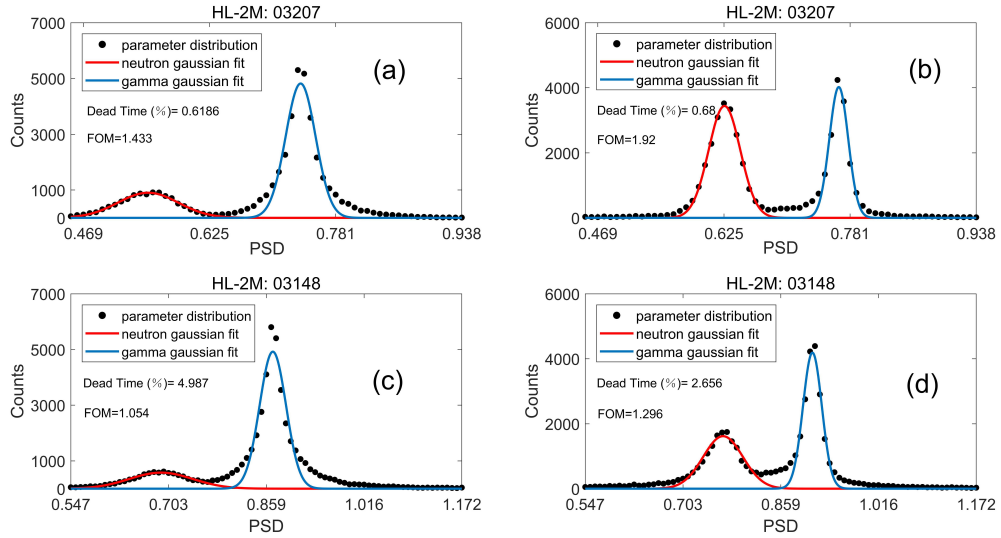


Fig. 13: PSD distributions using BC-501A (a) and EJ-309 (b) from discharge #03207. PSD distributions using BC-501A (c) and EJ-309 (d) from discharge #03148.

efficiency than BC-501A. However, both were weaker than the FC. The neutron count rate of BC-501A from discharge #03148 reached a maximum of 162 kcps, whereas that of EJ-309 reached 230 kcps.

The neutron count rate obtained with the NGDS exhibited the same variational trend as those obtained with the HTRN_S,

FC, and ³He. Thus, the NGDS is suitable for high-flux neutron measurements.

4.2.3. Neutron and gamma time trace comparison

Because of the additional shielding of EJ-309, the neutron count rate of EJ-309 in #03207 was larger than the gamma count rate from 1500 ms to 1600 ms. However, the gamma count rate of BC-501A was approximately 2–3 times higher than its neutron count rate during the same period. The situation in #03148 was similar to that in #03207, with the maximum total (neutron and gamma) count rates of BC-501A and EJ-309 exceeding 1 Mcps and 400 kcps, respectively. The gamma count rate of BC-501A from 1560 ms to 1600 ms was significantly higher than that of EJ-309 [Fig. 12(b)]. This indicated that an additional shielding treatment significantly reduced the sensitivity of the liquid scintillator detector to gamma rays and was more conducive to neutron detection. It also showed that the NGDS could perform n/γ discrimination at high count rates. Better results were obtained when both the neutron and gamma count rates were approximately 200 kcps for EJ-309 (total count rate of approximately 400 kcps).

We believe that the variation problem of the count value of BC-501A at a high count rate can be primarily attributed to the following two factors: first, BC-501A does not have effective gamma shielding, and the pile-up rejection algorithm does not completely eliminate the pile-up situation; second, the gain offset of the PMT may be an important reason.

4.2.4. Neutron–gamma discrimination with varying count rate

Care must be taken because the measurement dead time of the NGDS increases with the maximum count rate, and the FOM value for n/γ discrimination decreases, as shown in Fig. 12(c)). This implies that discrimination worsens.

The PSD curves of detectors #03207 and #03148, shown in Fig. 13, indicate that the FOM values are 1.433 and 1.92 for BC-501A (a) and EJ-309 (b), respectively, in #03207. The FOM values are 1.054 and 1.296 for BC-501A (c) and EJ-309 (d) in #03148, respectively, indicating that the DAQ is equally capable of discriminating between neutrons and gamma rays at high count rates. Simultaneously, the BC-501A has a low neutron-to-gamma ratio owing to the lack of lead shielding,

and a lot of gamma-rays are identified. This may also have resulted in EJ-309 being discriminated better than BC-501A under the same discharge number.

5. DISCUSSION AND CONCLUSIONS

In this study, a digital neutron–gamma discrimination system coupled with two liquid scintillators was designed. Serial-to-parallel conversion and four-channel parallel processing were performed to satisfy the timing requirements of FPGA at a high sampling rate. After optimizing the measurement parameters, the experiment was conducted using an Am–Be neutron–gamma source. The system performed real-time n/γ discrimination with satisfactory results at a sampling rate of 500-Msps. The best FOM values of 1.3 (BC-501A) and 1.5 (EJ-309) were obtained at an energy threshold of 300 keV_{ee}.

In the HL-2M tokamak experiments, the NGDS counted neutrons at a higher count rate (higher neutron flux) and higher time accuracy (1 ms) than other types of neutron detectors, implemented real-time n/γ discrimination, and calculated the energy spectra of neutrons and gamma rays. These measurements exhibited good consistency with other neutron measurements in HL-2M, and at approximately 400 kcps for EJ-309, the electronics effectively discriminated between neutrons and gamma rays. The discrimination results of the two detectors at higher count rates must be further confirmed in future measurements, and the problem of the gamma count rate variation of BC-501A at high count rates must also be resolved and optimized.

The NGDS performed real-time measurement in two different modes: list mode and spectrum mode, which were applied to different situations. The list mode performed pulse information calculations, making the entire discrimination process more detailed; however, it is only suitable for measurements at lower count rates. The spectrum mode is suitable for high count rates and is expected to be useful for fusion neutron measurements in future HL-2M experiments.

Because of the flexible FPGA firmware structure, the parameters can be adjusted without drastic changes to the algorithm to accommodate other detectors to meet different neutron–gamma discrimination requirements in future measurements.

-
- [1] K. Khattab, Measurement of the fast neutron flux in the MNSR inner irradiation site. *Appl. Radiat. Isot.* **65** 46–49 (2007). <https://doi.org/10.1016/J.APRADISO.2005.11.020>
 - [2] K. Ogawa, M. Isobe, S. Sangaroon, E. Takada, T. Nakada, S. Murakami, J. Jo, G.Q. Zhong, Y. Zhang, S. Tamaki, I. Murata, Time-resolved secondary triton burnup 14 MeV neutron measurement by a new scintillating fiber detector in middle total neutron emission ranges in deuterium large helical device plasma experiments. *AAPPS Bull.* **31**, 20 (2021). <https://doi.org/10.1007/s43673-021-00023-2>
 - [3] J. Gregor, M. Baron, J. Kesten, E.A. Kroeger, Comparison of the response of handheld neutron detectors in differing deployment environments: Measurements, calculations, and practical implications, *Radiat. Meas.* **143**, 106571 (2021). <https://doi.org/10.1016/J.RADMEAS.2021.106571>
 - [4] Y. Lotfi, S.A. Moussavi-Zarandi, N. Ghal-Eh, E. Pourjafarabadi, E. Bayat, Neutron–gamma discrimination based on quantum clustering technique. *Nucl. Instruments and Methods Phys. Res. Sect. A Accel. Spectrometers, Detect. Assoc. Equip.* **928**, 51–57 (2019). <https://doi.org/10.1016/J.NIMA.2019.03.009>
 - [5] M. Hamel, A.M. Frelin-Labalme, S. Normand, The influence

- of the solvent in fast neutron/gamma discrimination. *Epl.* **106**, 52001 (2014). <https://doi.org/10.1209/0295-5075/106/52001>
- [6] M. Sénoville, F. Delaunay, M. Pärlog, N.L. Achouri, N.A. Orr, Neutron- γ discrimination with organic scintillators: Intrinsic pulse shape and light yield contributions. *Nucl. Instruments and Methods Phys. Res. Sect. A Accel. Spectrometers, Detect. Assoc. Equip.* **971**, 164080 (2020). <https://doi.org/10.1016/j.nima.2020.164080>
 - [7] G. Yuan, Z. Wen, L. Wei, J. Zhang, Q. Yang, Neutron yield measurement system of HL-2A tokamak. *Plasma Sci. Technol.* **24**, 064006 (2022). <https://doi.org/10.1088/2058-6272/ac4f40>
 - [8] R.J. Zhu, X. Zhou, Z.H. Liu, W. Di Wang, X.L. Mou, T.F. Fang, Q.L. Ma, X.F. Xu, G.L. Yuan, L. Zhao, L.F. Wei, Z.J. Yin, High-precision and wide-range real-time neutron flux monitor system through multipoint linear calibration. *Nucl. Sci. Tech.* **31**, 94 (2020). <https://doi.org/10.1007/s41365-020-00798-3>
 - [9] C. Guerrero, D. Cano-Ott, M. Fernández-Ordóñez, E. González-Romero, T. Martínez, D. Villamarín, Analysis of the BC501A neutron detector signals using the true pulse shape. *Nucl. Instruments and Methods Phys. Res. Sect. A Accel. Spectrometers, Detect. Assoc. Equip.* **597**, 212–218 (2008). <https://doi.org/10.1016/j.nima.2008.09.017>
 - [10] H. Bai, Z. Wang, L. Zhang, Y. Lu, H. Jiang, J. Chen, G. Zhang, Calibration of an EJ309 liquid scintillator using an AmBe neutron source. *Nucl. Instruments and Methods Phys. Res. Sect. A Accel. Spectrometers, Detect. Assoc. Equip.* **863**, 47–54 (2017). <https://doi.org/10.1016/j.nima.2017.04.028>
 - [11] M. Amiri, V. Přenosil, F. Cvachovec, Z. Matěj, F. Mravec, Quick algorithms for real-time discrimination of neutrons and gamma rays. *J. Radioanal. Nucl. Chem.* **303**, 583–599 (2015). <https://doi.org/10.1007/s10967-014-3406-5>
 - [12] K. Mitev, P. Cassette, Radioactive Noble Gas Detection and Measurement with Plastic Scintillators. https://doi.org/10.1007/978-3-030-73488-6_11
 - [13] C. Liao, H. Yang, Pulse shape discrimination using EJ-299-33 plastic scintillator coupled with a Silicon Photomultiplier array. *Nucl. Instruments and Methods Phys. Res. Sect. A Accel. Spectrometers, Detect. Assoc. Equip.* **789**, 150–157 (2015). <https://doi.org/10.1016/j.nima.2015.04.016>
 - [14] M.C. Recker, E.J. Cazalas, J.W. McClory, Pulse shape discrimination with a low-cost digitizer using commercial off-the-shelf components. *Nucl. Instruments and Methods Phys. Res. Sect. A Accel. Spectrometers, Detect. Assoc. Equip.* **954**, 161479 (2020). <https://doi.org/10.1016/j.nima.2018.10.157>
 - [15] J. Le Cai, D.W. Li, P.L. Wang, Z.M. Zhang, X.H. Li, B.T. Feng, T.T. Hu, T. Tong, W. Zhou, L. Wei, Fast pulse sampling module for real-time neutron–gamma discrimination. *Nucl. Sci. Tech.* **30**, 1–8 (2019). <https://doi.org/10.1007/s41365-019-0595-1>
 - [16] H. Ye, L. Chen, X. Xu, G. Jin, Fast FPGA algorithm for neutron–gamma discrimination. *Nucl. Instruments and Methods Phys. Res. Sect. A Accel. Spectrometers, Detect. Assoc. Equip.* **1027**, 166256 (2022). <https://doi.org/10.1016/j.nima.2021.166256>
 - [17] S.X. Liu, W. Zhang, Z.H. Zhang, S. Lin, H.R. Cao, C.X. Song, J.L. Zhao, G.Q. Zhong, Performance of real-time neutron/gamma discrimination methods. *Nucl. Sci. Tech.* **34**, 1–9 (2023). <https://doi.org/10.1007/s41365-022-01160-5>
 - [18] H.B. Yang, H. Su, J. Kong, K. Cheng, J. Da Chen, C.M. Du, J.Z. Zhang, Application of the DRS4 chip for GHz waveform digitizing circuits. *Chinese Phys. C.* **39**, 056101 (2015). <https://doi.org/10.1088/1674-1137/39/5/056101>
 - [19] A. Fernandes, N. Cruz, B. Santos, P.F. Carvalho, J. Sousa, B. Goncalves, M. Riva, F. Pollastrone, C. Centioli, D. Marocco, B. Esposito, C.M.B.A. Correia, R.C. Pereira, FPGA Code for the Data Acquisition and Real-Time Processing Prototype of the ITER Radial Neutron Camera. *IEEE Trans. Nucl. Sci.* **66**, 1318–1323 (2019). <https://doi.org/10.1109/TNS.2019.2903646>
 - [20] N. Cruz, B. Santos, A. Fernandes, P.F. Carvalho, J. Sousa, B. Goncalves, M. Riva, C. Centioli, D. Marocco, B. Esposito, C.M.B. Correia, R.C. Pereira, The Design and Performance of the Real-Time Software Architecture for the ITER Radial Neutron Camera. *IEEE Trans. Nucl. Sci.* **66**, 1310–1317 (2019). <https://doi.org/10.1109/TNS.2019.2907056>
 - [21] K. Ogawa, M. Isobe, T. Nishitani, T. Kobuchi, The large helical device vertical neutron camera operating in the MHz counting rate range. *Rev. Sci. Instrum.* **89**, 113509 (2018). <https://doi.org/10.1063/1.5054818>
 - [22] J. Zhang, Y. Zhang, J. Zhang, J. Zhou, X. Zhan, Z. Wen, S. Cheng, Y. Zhu, G. Yuan, Y. Liu, Q. Yang, W. Chen, Z. Shi, Y. Liu, M. Xu, Development of a high-temporal resolution neutron flux measurement system for the HL-2M tokamak. *J. Instrum.* **17**, P07027 (2022). <https://doi.org/10.1088/1748-0221/17/07/P07027>
 - [23] J. Zhang, X. Qin, M.Y. Zhao, X. Chen, FPGA implementation of a real-time digital pulse processing analysis for radiation detectors. *Appl. Radiat. Isot.* **176**, 109900 (2021). <https://doi.org/10.1016/j.apradiso.2021.109900>
 - [24] V.T. Jordanov, G.F. Knoll, Digital synthesis of pulse shapes in real time for high resolution radiation spectroscopy. *Nucl. Instruments and Methods Phys. Res. Sect. A Accel. Spectrometers, Detect. Assoc. Equip.* **345**, 337–345 (1994). [https://doi.org/10.1016/0168-9002\(94\)91011-1](https://doi.org/10.1016/0168-9002(94)91011-1)
 - [25] H. Yang, J. Zhang, J. Zhou, J. Fan, Efficient pile-up correction based on pulse-tail prediction for high count rates. *Nucl. Instruments and Methods Phys. Res. Sect. A Accel. Spectrometers, Detect. Assoc. Equip.* **1029**, 166376 (2022). <https://doi.org/10.1016/j.nima.2022.166376>
 - [26] Y. Kaschuck, B. Esposito, Neutron/ γ -ray digital pulse shape discrimination with organic scintillators. *Nucl. Instruments and Methods Phys. Res. Sect. A Accel. Spectrometers, Detect. Assoc. Equip.* **551**, 420–428 (2005). <https://doi.org/10.1016/j.nima.2005.05.071>
 - [27] M. Nakhostin, A comparison of digital zero-crossing and charge-comparison methods for neutron/ γ -ray discrimination with liquid scintillation detectors. *Nucl. Instruments and Methods Phys. Res. Sect. A Accel. Spectrometers, Detect. Assoc. Equip.* **797**, 77–82 (2015). <https://doi.org/10.1016/j.nima.2015.06.041>
 - [28] F.D. Brooks, R.W. Pringle, B.L. Funt, Pulse Shape Discrimination in a Plastic Scintillator. *IRE Trans. Nucl. Sci.* **7**, 35–38 (1960). <https://doi.org/10.1109/TNS.1960.4315733>
 - [29] R.A. Winyard, J.E. Lutkin, G.W. McBeth, Pulse shape discrimination in inorganic and organic scintillators. *I. Nucl. Instruments Methods.* **95**, 141–153 (1971). [https://doi.org/10.1016/0029-554X\(71\)90054-1](https://doi.org/10.1016/0029-554X(71)90054-1)
 - [30] S. Korolczuk, M. Linczuk, R. Romaniuk, I. Zychor, Development of a digital method for neutron/gamma-ray discrimination based on matched filtering. *J. Instrum.* **11**, C09013 (2016). <https://doi.org/10.1088/1748-0221/11/09/C09013>
 - [31] H. Klein, S. Neumann, Neutron and photon spectrometry with liquid scintillation detectors in mixed fields. *Nucl. Instruments and Methods Phys. Res. Sect. A Accel. Spectrometers, Detect. Assoc. Equip.* **476**, 132–142 (2002). [https://doi.org/10.1016/S0168-9002\(01\)01410-3](https://doi.org/10.1016/S0168-9002(01)01410-3)
 - [32] H. Singh, R. Mehra, Discrete Wavelet Transform Method

- for High Flux n - γ Discrimination with Liquid Scintillators. *IEEE Trans. Nucl. Sci.* **64**, 1927–1933 (2017). <https://doi.org/10.1109/TNS.2017.2708602>
- [33] X. Zhu, C. Feng, Q. Li, Z. Shen, S. Liu, Q. An, FPGA-Based Real-Time n/γ Discrimination with Liquid Scintillator. *IEEE Trans. Nucl. Sci.* **65**, 2877–2882 (2018). <https://doi.org/10.1109/TNS.2018.2877598>
- [34] Y.P. Zhang, J.W. Yang, Y. Liu, T.S. Fan, X.B. Luo, G.L. Yuan, P.F. Zhang, Development of the radial neutron camera system for the HL-2A tokamak Development of the radial neutron camera system for the HL-2A tokamak. *Rev. Sci. Instrum.* **87**, 063503 (2016). <https://doi.org/10.1063/1.4953109>